Improved Measurement Method of Material Properties Using Continuous Cavity Perturbation Without Relocation

Chul-Ki Kim, Laxmikant Minz, and Seong-Ook Park, *Senior Member, IEEE*

***Abstract*— Depolarized fields inside a magnetodielectric sample interfere with the accurate measurement of sample characteristics in a cavity perturbation method. These depolarized fields occur due to the polarization of the test sample, depending on the volume and shape of the sample, in the electromagnetic field. To characterize the magnetodielectric sample more accurately, we proposed an advanced rectangular cavity (RC) perturbation method. In this method, we investigated the change in the resonant frequency and *Q*-factor of a cavity which depends on the volume, and shape of the sample, and depolarized fields within the sample. The depolarizing factor for calculating the permittivity and permeability of the sample is derived by separating the uniform and depolarized fields within the sample when the sample is inserted in the cavity. These separations of fields play an important role to improve the measurement accuracy. The proposed unified RC perturbation technique is validated initially by measuring the resonant frequency and quality factor and then calculating the complex permittivity and permeability at the TE_{10l} mode. The standard dielectric material (Al_2O_3) and magnetic material (YIG) samples are measured with the vector network analyzer. The measurement was performed when the magnetodielectric sample having various shapes and volumes inserted into the RC resonator. In comparison with the previous cavity perturbation methods, the permittivity and permeability have been calculated more accurately with various shapes of the test sample, and we also found that the ratio of the maximum sample volume to the cavity for various samples increases about 40%. Based on the proposed method, for a cube-shaped sample, we obtained the complex permittivity and permeability consecutively at each resonance mode without any physical relocation of the test sample. Therefore, the test sample is capable of continuous more accurate and more effective measurement in the desired frequency band without relocation using the proposed technique.**

***Index Terms*— Cavity perturbation technique (CPT), complex permeability, complex permittivity, Q-factor, resonator.**

I. Introduction

MEASUREMENT method for complex permittivity ($\varepsilon_r^* = \varepsilon_r' - j\varepsilon_r''$) and complex permeability ($\mu_r^* = \mu_r' - j\mu_r''$) of magnetodielectric materials using resonant cavity perturbation has been established and improved progressively in the microwave and RF engineering. The cavity perturbation technique (CPT) is the most common resonator-based approach for the characterization of magnetodielectric materials that have a homogenous and isotropic structure at microwave frequencies [1]–[25]. The conventional CPT formulas for measuring material properties can be derived from Maxwell's equations mentioned in [1]. It is well known that the complex permittivity of dielectric samples is obtained in the maximum *E*-plane of the cavity, whereas the complex permeability of the magnetic sample is obtained in the maximum *H*-plane of the cavity. Moreover, in the rectangular cavity (RC), the test sample is placed vertically in the electric field and horizontally in the magnetic field [1], [2]. However, it has been reported that the polarized field occurs in cavity, which disturbs the sample characteristics measurement [12], [13], [17], [21], [26]. When the test sample is inserted and placed at the maximum field position of cavity in the presence of electric or the magnetic fields, the sample gets partially polarized and the degree of polarization varies with the sample dimension. Hence, the effective volume and polarized field of the test sample significantly influence the accuracy of measurements inside the cavity. Therefore, in order to maintain the accuracy in the earlier CPTs, the test sample should be specific rod or bar-shape, which equals the height of the cavity to decrease the interference of the polarization. Many previous researchers have proposed various ways to measure more accurate properties of the sample positioned at the maximum electromagnetic field [11]–[16].

In this article, our objective is to address the possible solution to determine the complex permittivity and the complex permeability of materials mathematically more accurately and compare the results between the proposed and conventional CPT formulas using the simulations and experiment. In this article, we adopt an RC resonator where the transverse electric (TE) mode is dominant as per the resonance frequency equation [1]. The conventional RC formulas to evaluate the complex permittivity and the complex permeability have been improved and modified to suit all shapes and dimensions of the sample. A previous work on CPT integrates the electromagnetic fields of cavity and polarization inside the sample [3]–[5], [12], [13], [16], [17]. However, in our approach, we modified and improved the formulas to correct and separate the polarized field and original field inside the sample. Moreover, we define the valid volume and depolarization factor according to the various shapes of the sample. Then, applying them to

Manuscript received August 9, 2019; revised December 16, 2019; accepted December 29, 2019. Date of publication January 14, 2020; date of current version June 24, 2020. This work was supported by the Basic Science Research Program through the National Research Foundation of Korea (NRF) funded by the Ministry of Science, ICT & Future Planning under Grant NRF-2019R1A2B5B01069407. The Associate Editor coordinating the review process was Seyed Hossein Sadeghi. *(Corresponding author: Chul-Ki Kim.)*

The authors are with the Microwave and Antenna Laboratory, Department of Electrical Engineering, Korea Advanced Institute of Science and Technology, Daejeon, South Korea (e-mail: chulki@kaist.ac.kr; lkminz@kaist.ac.kr; soparky@kaist.ac.kr).

Color versions of one or more of the figures in this article are available online at http://ieeexplore.ieee.org.

Digital Object Identifier 10.1109/TIM.2020.2966358

the perturbation theory, we evaluated the modified CPT. The accuracy of the characterization of reference magnetodielectric sample properties of different shapes and volumes through the CPT measurement has been verified using the vector network analyzer (VNA). The purpose of this article is to demonstrate that the new technique can measure more accurately and easily the complex permittivity and permeability than the conventional CPT. This article is organized as follows. Section II discusses the conventional cavity perturbation formulas to determine complex permittivity and permeability of materials along the E- and H-planes. Section III introduces an advanced rectangular CPT, in which modification and improvement are applied by considering the effect of depolarization on the test magnetodielectric samples. To prove the proposed method, Section IV explains the maximum volume of the test sample having different shapes and sizes in simulation. The practical experiment and results on real data have been reported and discussed in Section V. Finally, we apply our method to a new measurement idea in Section VI, followed by the conclusion in Section VII.

II. Theoretical Background

The perturbation equation is derived from Maxwell's equation [1]

$$\frac{\Delta\omega}{\omega_0} = \frac{-\int_{V_S}(\Delta\varepsilon\overline{E}\cdot\overline{E}_0^* + \Delta\mu\overline{H}\cdot\overline{H}_0^*)dV}{\int_{V_C}(\overline{D}_0\cdot\overline{E}_0^* + \overline{B}_0\cdot\overline{H}_0^*)dV} \tag{1}$$

where $\Delta\omega = \omega_s - \omega_0$ is the complex resonant frequency shift between the complex resonant frequency of the cavity with the sample (ω_s) and without the sample (ω_0). Here, $\overline{E}_0$ and $\overline{H}_0$ are the electric and magnetic fields in the cavity without the sample, while $\overline{E}$ and $\overline{H}$ are the electric and magnetic fields in the cavity with the sample. The volume integral over term $\overline{H}_0$ and $\overline{B}_0$ in the denominator is absorbed as a factor of 2 because the time average of the energy is twice the energy stored in the electric field [6]. In the maximum E-plane, the terms with $\overline{H}_0$ in the numerator vanish, whereas, in the maximum H-plane, the terms with $\overline{E}_0$ in the numerator also vanish. The general expression of the CPT formula available in the literature for the microwave material properties' calculation [1], [2]

$$\frac{\omega_s - \omega_0}{\omega} = -\frac{(\varepsilon_r^* - 1)\int_{V_S}(\overline{E}\cdot\overline{E}_0^*)dV}{2\int_{V_C}\left|\overline{E}_0\right|^2 dV} \tag{2}$$

$$\frac{\omega_s - \omega_0}{\omega} = -\frac{(\mu_r^* - 1)\int_{V_S}(\overline{H}\cdot\overline{H}_0^*)dV}{2\int_{V_C}\left|\overline{H}_0\right|^2 dV} \tag{3}$$

where $\varepsilon_r^* = \varepsilon_r' - j\varepsilon_r''$ *and* $\mu_r^* = \mu_r' - j\mu_r''$ are the complex properties of the sample under the measurement. The variables V_s and V_c represent the volume of the sample and those of the cavity, respectively. The complex resonant frequency can be separated into the real and imaginary parts as [1], [3]

$$\frac{\omega_s - \omega_0}{\omega} = \frac{f_s - f_0}{f_0} + \frac{j}{2}\left(\frac{1}{Q_S} - \frac{1}{Q_0}\right) \tag{4}$$

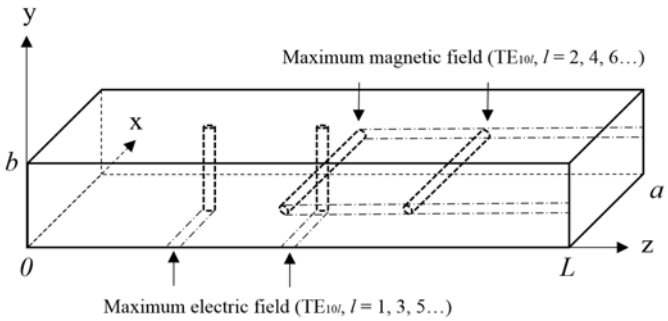

Fig. 1. Example of the finite-volume sample placed in the maximum electromagnetic field of the TE_{10l} mode inside the *RC*.

where f_0 and Q_0 are the resonant frequency and the quality factor of the unperturbed cavity, while f_s and Q_s represent the corresponding parameters for the perturbed cavity, respectively. The formulas, proposed in the literature [3]–[5] to calculate the complex permittivity and permeability of the sample placed vertically and horizontally in the RC, are the classic perturbation method formulas given as

$$\begin{aligned}\varepsilon_r' &= 1 + \frac{1}{2}\left(\frac{f_0 - f_s}{f_0}\right)\frac{V_C}{V_S}\\ \varepsilon_r'' &= \frac{1}{4}\left(\frac{1}{Q_S} - \frac{1}{Q_0}\right)\frac{V_C}{V_S}\end{aligned} \tag{5}$$

$$\begin{aligned}\mu_r' &= 1 + \left(\frac{\lambda_g^2 + 4a^2}{8a^2}\right)\left(\frac{f_0 - f_s}{f_0}\right)\frac{V_C}{V_S}\\ \mu_r'' &= \left(\frac{\lambda_g^2 + 4a^2}{16a^2}\right)\frac{V_C}{V_S}\left(\frac{1}{Q_S} - \frac{1}{Q_0}\right)\end{aligned} \tag{6}$$

where $\lambda_g = (2\pi/\beta)$ and a is the width of RC. Equations (5) and (6) are derived, assuming that the test sample has full length as of the cavity and has an infinitesimally small thickness.

The measurement structure shown in Fig. 1 can be considered as the classic cavity perturbation measurement. However, the accuracy of the classic CPT formulas (5) and (6) cannot be trusted in different conditions of inserted samples. In other words, the accuracy of these equations requires the following conditions.

1) The sample length is equal to the height or width of the RC when placed vertically or horizontally, respectively.
2) The sample volume should be infinitesimally small.
3) The sample should be located at the maximum E-field and maximum H-field for complex permittivity and complex permeability, respectively.

If these conditions are not satisfied, then the validity of the assumptions $\overline{E} = \overline{E_0}$ and $\overline{H} = \overline{H_0}$ will no longer be true. It can increase the uncertainty in the measurement for complex properties of a material. Therefore, the field variation over the sample must be considered, if the aforementioned conditions are not met, for the accurate permittivity and permeability measurement of magnetodielectric samples [11], [29].

Section III considers the above-mentioned problems of the classic CPT, and consequently, we derive the modified form of the closed-form expressions to define the complex permittivity

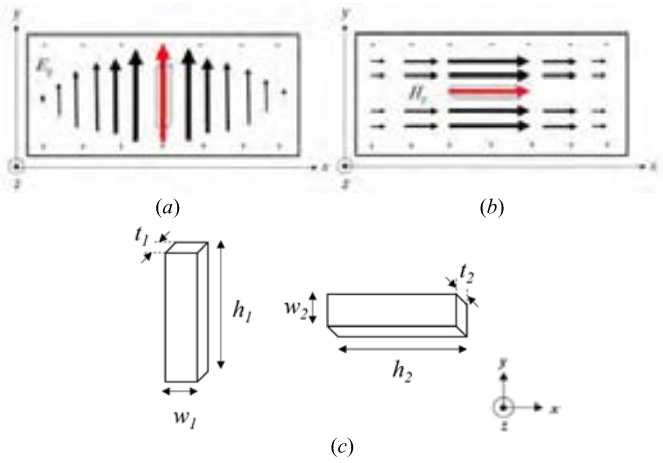

Fig. 2. Side view of the sample position placed in (a) E-plane and (b) H-plane. (c) Sample dimensions are t, h, and w for thickness, height, and width, respectively. First sample dimension is to measure the complex permittivity and next sample dimension is to measure the complex permeability.

and permeability of various samples placed in the E- and H-planes of the RC.

III. Advanced Cavity Perturbation Method

When the sample is inserted in the E- and H-planes of the RC, the electromagnetic field variation occurs vertically or horizontally. Due to this phenomenon, we can estimate the accurate characterization of material properties based on the direction and scale of the field variation. Therefore, the sample position is very important. Since the position of the sample, shown in Fig. 1, only perturbs the E_y and H_x components in the maximum electric and magnetic fields, this position is usually chosen to achieve the maximum sensitivity in measuring the complex permittivity and permeability [2].

The classic formulas (5) and (6) does not consider the effect of electric and magnetic field variations over different positions of the test sample. To solve this issue and to calculate the accurate sample properties in various sizes and shapes of the sample, here, we investigate three points: valid sample volume influenced by the electromagnetic field, field variations due to the partially polarized field within the sample, and an ideal electric or magnetic field from the RC.

A. Valid Sample Volume in the Electromagnetic Field

First, the valid sample volume is calculated from the numerator of (2) and (3). It is observed in Fig. 2 that the tangential field is having sinusoidal variation along the x-axis. Similarly, there will be a sinusoidal field variation in the z-axis. These sinusoidal variation analyses are not considered by the classic formulas (5) and (6). The valid volume of the finite sample can be integrated by the induced electromagnetic field at the maximum electric and magnetic fields, respectively, which result in the following equation:

$$V_S' = \int_{\frac{a}{2}-\frac{t_1}{2}}^{\frac{a}{2}+\frac{t_1}{2}} \int_{\frac{b}{2}-\frac{h_1}{2}}^{\frac{b}{2}+\frac{h_1}{2}} \int_{\frac{L}{2}-\frac{w_1}{2}}^{\frac{L}{2}+\frac{w_1}{2}} \sin^2\left(\frac{\pi x}{a}\right) \sin^2(\beta z)\, dx dy dz \tag{7}$$

$$V_S' = \int_{\frac{a}{2}-\frac{h_2}{2}}^{\frac{a}{2}+\frac{h_2}{2}} \int_{\frac{b}{2}-\frac{w_2}{2}}^{\frac{b}{2}+\frac{w_2}{2}} \int_{\frac{L}{2}-\frac{t_2}{2}}^{\frac{L}{2}+\frac{t_2}{2}} \sin^2\left(\frac{\pi x}{a}\right) \cos^2(\beta z)\, dx dy dz \tag{8}$$

where w_1, t_1, h_1, w_2, t_2, and h_2 are the sample dimension [see Fig. 2(c)]. The parameters of a, b, and L are the dimension of cavity resonator, as shown in Fig. 1. Equations (7) and (8) indicate the integral equations at the maximum electric and magnetic fields, respectively. For all positions inside the RC, we need to redefine the sample volume at the resonant location according to the field. The electric and magnetic fields' configuration of the TE_{10l} mode from standing waves inside the RC shown in Fig. 1 can be derived to have the following nonzero field components. H_x, E_y, and H_z are each dominant field in the x-, y-, and z-directions of the TE_{10l} mode, respectively [2]

$$\begin{aligned} E_y &= E_0 \sin\left(\frac{\pi x}{a}\right) \sin(\beta z) \\ H_x &= -\frac{\beta a}{\pi} C \sin\left(\frac{\pi x}{a}\right) \cos(\beta z) \\ H_z &= C \cos\left(\frac{\pi x}{a}\right) \sin(\beta z) \end{aligned} \tag{9}$$

where $C = (j\pi/k\eta a)E_0, \beta = (l\pi/L)$, E_0 is the maximum amplitude of the electric field at the resonant point shown in Fig. 2(a), a and b are the length of xy section in the RC, and L is the length of the cavity along the z-direction. The symbol *"l"* represents the z-directional orders of the pattern in the TE_{10l} mode ($l = 1, 2, 3, \ldots$). Considering the fields (9) that vary depending on the position of RC, we integrate (7) and (8) in accordance with the tangential field. The valid sample volume affected by the field variation can be obtained when the sample is partially placed in the maximum electric and magnetic fields

$$V_S' = h_1 \left(\frac{w_1}{2} + \frac{a}{2\pi} \sin\left(\frac{\pi w_1}{a}\right)\right) \left(\frac{t_1}{2} + \frac{L}{2\pi l} \sin\left(\frac{l\pi t_1}{L}\right)\right) \tag{10}$$

$$V_S' = \frac{w_2 t_2 h_2}{4} \left(1 + \frac{\sin(k_x h_2)}{k_x h_2}\right) \left(1 + \frac{\sin(k_z t_2)}{k_z t_2}\right) \tag{11}$$

where $k_x = \pi/a, k_z = (l\pi/L)$, and l is the TE_{10l} resonant mode number. Formulas (10) and (11) are the calculation results when the bar-type sample is located around the center of the rectangular resonator [8]–[11]. For the full-length sample having infinitesimally small thickness, the modified formulas (10) and (11) simplified to the original volume of the sample ($Vs = w \times t \times h$). Furthermore, by utilizing these final modified rectangular CPT equations, we are able to estimate the maximum sample volume to the cavity ratio, which will be discussed in Section IV, and then, we can verify the effective volumes by the measurement to the various samples in Section V.

B. Polarized Field in the Sample and Ideal Field From RC

Complex permittivity and permeability of a magnetodielectric sample can be determined by the classic CPT when the test sample length equals the length of RC. However, if the test sample length is shorter or the sample is not rod/bar shape, then the classic CPT is not applicable. This is due to the

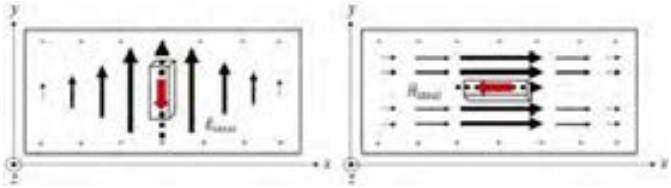

Fig. 3. Depolarization of the sample in the applied field from RC.

partially polarized field within the sample by the applied field from the RC. Then, new electric and magnetic fields for complex permittivity and permeability must be derived. Recently, some researchers reported an idea to solve the problem of the classic CPT [12], [13]. They evaluated the total vector sum of the applied field and the depolarizing field. Different from the previous article, we divide the field variation into two parts and analyzed them individually. One part is the ideal field from the RC, and the other part is the polarized field in the sample. This approach adds more accuracy to the calculation of magnetodielectric sample properties and first step to go beyond the limit of the classic CPT

$$\overline{E} = \overline{E}_{\text{ideal}} - \overline{E}_p$$
$$\overline{D} = \overline{D}_{\text{ideal}} - \overline{D}_p \tag{12}$$
$$\overline{H} = \overline{H}_{\text{ideal}} - \overline{H}_p$$
$$\overline{B} = \overline{B}_{\text{ideal}} - \overline{B}_p \tag{13}$$

where subscript "ideal" indicates the ideal field inside the sample from RC and subscript "p" indicates the polarized field inside the sample from RC. It can be noted in Fig. 3 that the polarized field in the sample will point in the opposite direction to the applied electric field called depolarization. Therefore, the polarized field is subtracted from the ideal field in the sample. The electric ideal field and the depolarization field can be calculated. The displacement field is obtained by multiplying the permittivity of free space (ε_0), the complex permittivity of the sample (ε_r^*), and the electric field ($\overline{E}_{\text{ideal}}$) from RC. It can be expressed as [1]

$$\overline{D}_{\text{ideal}} = \varepsilon_0 \varepsilon_r^* \overline{E}_{\text{ideal}}. \tag{14}$$

The polarized field can be calculated from the polarization magnitude, which is depolarizing factor (N). In a linear medium, the electric polarization is linearly related to the applied electric field as [13]

$$\overline{E}_p = \frac{NP}{\varepsilon_0} \tag{15}$$
$$P = \varepsilon_0(\varepsilon_r^* - 1)\overline{E}_s \tag{16}$$

where P is the polarization magnitude, $\overline{E}_p$ is the polarized electric field, and $\overline{E}_s$ is the total electric field that is the sum of the ideal field and the polarized field. After substituting the total electric field inside the sample, we can get

$$\overline{E}_s = \overline{E}_{\text{ideal}} - \overline{E}_p = \frac{1}{1 + N(\varepsilon_r^* - 1)}\overline{E}_{\text{ideal}}. \tag{17}$$

Therefore, the polarized displacement field can be finally calculated as

$$\overline{D}_p = \varepsilon_0 \varepsilon_r^* \overline{E}_p = \varepsilon_0 \varepsilon_r^* \frac{N(\varepsilon_r^* - 1)}{1 + N(\varepsilon_r^* - 1)}\overline{E}_{\text{ideal}}. \tag{18}$$

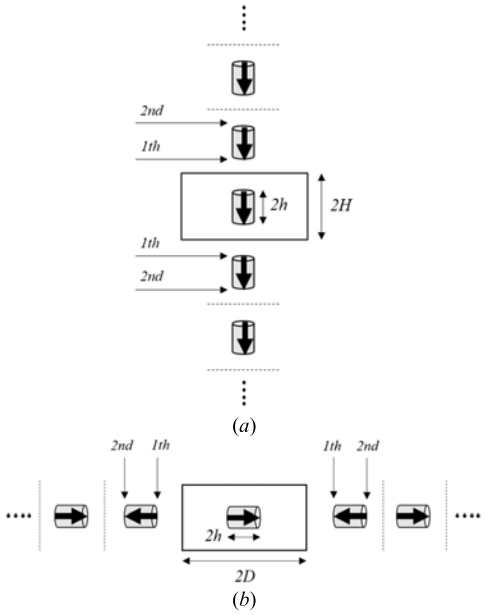

Fig. 4. Formation of (a) image dipoles in the electric field [16] and (b) image dipoles in the magnetic field.

Likewise, the magnetic ideal field and the depolarization field can be evaluated. The magnetic flux density is obtained by multiplying the permeability of free space, the complex permeability of the sample, and the magnetic field from RC [1]

$$\overline{B}_{\text{ideal}} = \mu_0 \mu_r^* \overline{H}_{\text{ideal}}. \tag{19}$$

Moreover, the polarized magnetic field can be obtained as starting from (20) [16], [17]

$$\overline{H}_p = NM \tag{20}$$
$$M = (\mu_r^* - 1)\overline{H}_s \tag{21}$$
$$\overline{H}_s = \overline{H}_{\text{ideal}} - \overline{H}_p = \frac{1}{1 + N(\mu_r^* - 1)}\overline{H}_{\text{ideal}} \tag{22}$$
$$\overline{B}_p = \mu_0 \mu_r^* \overline{H}_p = \mu_0 \mu_r^* \frac{N(\mu_r^* - 1)}{1 + N(\mu_r^* - 1)}\overline{H}_{\text{ideal}}. \tag{23}$$

The parameter of the depolarizing factor N depends on the geometrical dimension of the sample and has been evaluated as [14]–[16]

$$N_i = \int_0^\infty \frac{(x_1 y_1 z_1)du}{2(u + i^2)\sqrt{(u + x_1^2)(u + y_1^2)(u + z_1^2)}}$$
$$i = x_1, y_1, z_1 (x, y, z - \text{direction}). \tag{24}$$

Based on (24), we can define and apply the value of factor N according to the proportion of the length in the x-, y-, and z-directions.

Because the RC is surrounded by perfect electric conducting (PEC) walls, there will be the effects of images of depolarizing field to the cavity [16]. Fig. 4(a) and (b) shows the successive position of the electric and magnetic dipoles on the rectangular conducting walls. The electric field of dipoles occurred and generated the successive images on conducting wall, as reported in [16], can be defined as effective depolarizing factor N_e in the electric field. However, in the magnetic field

of a dipole, there are the opposite direction of fields on the conducting wall [1]. Hence, the effective depolarizing factor N_m is likely to get modified, especially when the length of the sample is less than the width of the cavity. When the length and the cross-sectional area of the sample are $2h$ and A, respectively, and the width of cavity is $2D$, the magnitude of the magnetic polarization of image dipoles (first, second, $\cdots$) has the format shown as

$$M_1 = \frac{M_{\text{ideal}} V_S}{A(4D-2h)}, \quad M_2 = \frac{M_{\text{ideal}} V_S}{A(4D+2h)} \cdots$$

Due to the sum of the sample polarization and its image dipoles, the depolarization field ($\overline{H}_p$) can be calculated as

$$\begin{aligned}
&\overline{H}_p \\
&= -N\overline{M}_{\text{ideal}}\left(1+\frac{h}{2D-h}-\frac{h}{2D+h}+\frac{h}{4D-h}-\frac{h}{4D+h}\cdots+\infty\right) \\
&= -N\overline{M}_{\text{ideal}} - N\overline{M}_{\text{ideal}} h \sum_{n=0}^{\infty}\left(\frac{1}{(2n+2)D-h}-\frac{1}{(2n+2)D+h}\right) \\
&= -N\overline{M}_{\text{ideal}}\left[1-\frac{1}{2}\left(\frac{h}{D}\right)^2 \sum_{n=1}^{\infty}\frac{1}{\left(\frac{h}{2D}\right)^2-n^2}\right]
\end{aligned}$$

using the standard mathematical series of [27]

$$\sum_{n=1}^{\infty}\left(\frac{1}{z^2-n^2}\right) = \frac{\pi}{2z}\cot(\pi z) - \frac{1}{2z^2}$$

leads to

$$\overline{H}_p = -N\left[2-\frac{h\pi}{2D}\cot\left(\frac{h\pi}{2D}\right)\right] M_{\text{ideal}}. \tag{25}$$

Comparing (25) with (24), the effective depolarizing factor N_m in the magnetic field can be changed. Therefore, the effective depolarizing factor in the electric and magnetic fields can be written as

$$N_e = N\frac{\pi h}{2H}\cot\frac{\pi h}{2H}, \quad N_m = N\left[2-\frac{\pi h}{2D}\cot\frac{\pi h}{2D}\right]. \tag{26}$$

C. Modified Cavity Perturbation Method

For improving the problem of classical CPT, we evaluated the characterization of sample volume in the maximum field and separated the depolarization field from the ideal field. The modified conventional reported formulas (2) and (3) at the maximum E- and H-fields can be written as

$$\frac{\omega_s-\omega_0}{\omega} = \frac{\left(\frac{1}{\varepsilon_r^*}-1\right)\int_{V_S}\overline{E}_{\text{ideal}}\cdot\left(\overline{D}_s^{\text{ideal}}-\overline{D}_s^{p}\right)dV}{2\varepsilon_0\int_{V_C}|E_{\text{ideal}}|^2 dV} \tag{27}$$

$$\frac{\omega_s-\omega_0}{\omega} = \frac{\left(\frac{1}{\mu_r^*}-1\right)\int_{V_S}\overline{H}_{\text{ideal}}\cdot\left(\overline{B}_s^{\text{ideal}}-\overline{B}_s^{p}\right)dV}{2\mu_0\int_{V_C}|H_{\text{ideal}}|^2 dV} \tag{28}$$

where the subscript s indicates the field or frequency after inserting the sample, and superscripts ideal and p indicate the original and polarized fields from the RC, respectively. By equating the real and imaginary parts on each side of (27) and (28), we obtain the final modified formulas shown in Appendix B for measuring accurate complex permittivity and permeability of magnetodielectric materials. Equations (29) and (30) are simplified from the equations in Appendix B. Derived formulas (29) and (30) have better accuracy for characterizing the properties of materials for complex permittivity and complex permeability, respectively

$$\begin{aligned}
\frac{f_0-f_s}{f_0} &= \left[(\varepsilon_r'-1) - \boldsymbol{EP_{real}}\right]2\frac{V_S'}{V_C} \\
\frac{1}{Q_S}-\frac{1}{Q_0} &= 4\frac{V_S'}{V_C}\left[\varepsilon_r'' - \boldsymbol{EP_{imag}}\right]
\end{aligned} \tag{29}$$

$$\begin{aligned}
\frac{f_0-f_s}{f_0} &= \left[(\mu_r'-1) - \boldsymbol{HP_{real}}\right]\frac{8a^2}{4a^2+\lambda_g^2}\frac{V_S'}{V_C} \\
\frac{1}{Q_S}-\frac{1}{Q_0} &= \left[\mu_r'' - \boldsymbol{HP_{imag}}\right]\frac{16a^2}{4a^2+\lambda_g^2}\frac{V_S'}{V_C}
\end{aligned} \tag{30}$$

where EP_{real} and EP_{imag} are the calculated terms for the real and imaginary parts, respectively, to adjust the error rate of the complex electrical property of a material. Likewise, HP_{real} and HP_{imag} are the calculated terms for the real and imaginary parts of the complex magnetic property. In addition, it is noted that (29) and (30) can also be simplified to the original cavity perturbation formulas by applying the aforementioned preconditions. Therefore, if effective depolarizing factor goes to zero, (29) and (30) are reduced as

$$\begin{aligned}
\lim_{N_e\to 0}\frac{f_0-f_s}{f_0} &= (\mu_r'-1)2\frac{V_S'}{V_C'} \\
\lim_{N_m\to 0}\frac{f_0-f_s}{f_0} &= (\mu_r'-1)\frac{8a^2}{4a^2+\lambda_g^2}\frac{V_S'}{V_C'}
\end{aligned} \tag{31}$$

$$\begin{aligned}
\lim_{N_e\to 0}\frac{1}{Q_S}-\frac{1}{Q_0} &= 4\varepsilon_r''\frac{V_S'}{V_C'} \\
\lim_{Nm\to 0}\frac{1}{Q_S}-\frac{1}{Q_0} &= \mu_r''\frac{16a^2}{4a^2+\lambda_g^2}\frac{V_S'}{V_C'}.
\end{aligned} \tag{32}$$

In Section IV, to prove the improvement of our method, we show the simulation results compared with the previous research, using the MATLAB and Computer Simulation Technology (CST) microwave studio for determining the maximum sample volume ratio to the cavity. Then, we analyze the practical experiment on real data to calculate the accurate complex permittivity and permeability of the various test samples by utilizing the proposed rectangular CPT.

IV. Simulation Results for Proposed Method (Maximum Volume of Sample)

It is important that we know the maximum sample volume to evaluate the complex properties of the sample in CPT accurately. If the sample can be measured in a wider volume range, we can measure the complex properties of different kinds of material more easily. The maximum volume range of the sample having various geometries with complex permittivity has already been evaluated in [12] by considering only the real parts and assuming the frequency shift range condition $[(f_0-f_s)/f_0 \le 10^{-3}]$

$$\frac{f_0-f_s}{f_0} = 2\cdot\frac{V_S}{V_C}\cdot\frac{N(\varepsilon_r'^2+\varepsilon_r''^2)+(1-2N)\varepsilon_r'^2+N-1}{(N\varepsilon_r'-N+1)^2+(N\varepsilon_r'')^2} \le 10^{-3}. \tag{33}$$

We can calculate the feasible maximum sample volume ratio $(V_s'/V_c)_{\max}$ in our proposed rectangular CPT using (33) and compare with the maximum sample volume ratio as reported in [12]. By equating the real part of (29) and assuming the same frequency shift range condition as in [12], it can be written as

$$\frac{f_0 - f_s}{f_0} = (\varepsilon_r' - 1)2\frac{V_S'}{V_C} - \frac{2N_e\left[\left((\varepsilon_r'-1)^2 - \varepsilon_r''^2\right)\left(N_e\varepsilon_r' - N_e + 1\right) + 2\left(\varepsilon_r' - 1\right)\varepsilon_r''^2 N_e\right]}{\left(N_e\varepsilon_r' - N_e + 1\right)^2 + \varepsilon_r''^2 N_e^2} \times \frac{V_S'}{V_C} \le 10^{-3}.$$

Thus, the ratio of maximum sample volume to cavity volume $(V_s/V_c)_{\max}$ is given by

$$\frac{V_S'}{V_C} = \frac{1}{2000\left[(\varepsilon_r' - 1) - \frac{N_e\left[\left((\varepsilon_r'-1)^2 - \varepsilon_r''^2\right)\left(N_e\varepsilon_r' - N_e + 1\right) + 2(\varepsilon_r'-1)\varepsilon_r''^2 N_e\right]}{\left(N_e\varepsilon_r' - N_e + 1\right)^2 + \varepsilon_r''^2 N_e^2}\right]}. \quad (34)$$

By using (34), the ratio of maximum sample volume to the cavity volume can be optimized by the MATLAB program as a function of real and imaginary parts of complex permittivity employing the proposed rectangular CPT. Fig. 5 shows the sample volume ratio $(V_s/V_c)_{\max}$ with the different sample shapes of dielectric rod/bar ($h = b$), disk/strip, and sphere/cube. It can be noticed from the simulated results that the ratio $(V_s/V_c)_{\max}$ increases or decreases with the complex permittivity values. In comparison to the previous investigation [12], the increase in ratio $(V_s/V_c)_{\max}$ can be seen, for the three different geometries of the sample. To compare the numerical increase with the article [12] in Fig. 5, we evaluate the comparison of $(V_s/V_c)_{\max}$ with low-loss $Al_2O_3(\varepsilon_r^* = 8.9 - 0.004i$ at 2.45 GHz) [18] and high-loss SiC ($\varepsilon_r^* = 26.66 - 27.99i$ at 2.45 GHz) [19] in Table I. The increased rate of the ratio $(V_s/V_c)_{\max}$ is following the order with different geometries of the same material: sphere/cube > rod/bar > strip/disk. It is observed that $(V_s/V_c)_{\max}$ is increased up to almost 40% in the example geometries except for the strip/disk. In the case of strip/disk, the dielectric material has the N value equal to "1." It means that the material is sufficiently polarized as the capacitor in the electric field. Therefore, when the disk-shaped sample is sufficiently polarized, then the reported CPT [12] can also be useful. However, if the sample has other shape, then we should consider an alternative method to improve the accuracy. Therefore, we address various shapes of samples for our proposed rectangular CPT in this article.

Likewise, the maximum volume range of the sample having various geometries with complex permeability can also be obtained by applying the frequency shift range condition $[(f_0 - f_s)/f_0 \le 10^{-3}]$. TE105 resonance mode is arbitrarily selected for simulation. We consider the magnetite CPT, which

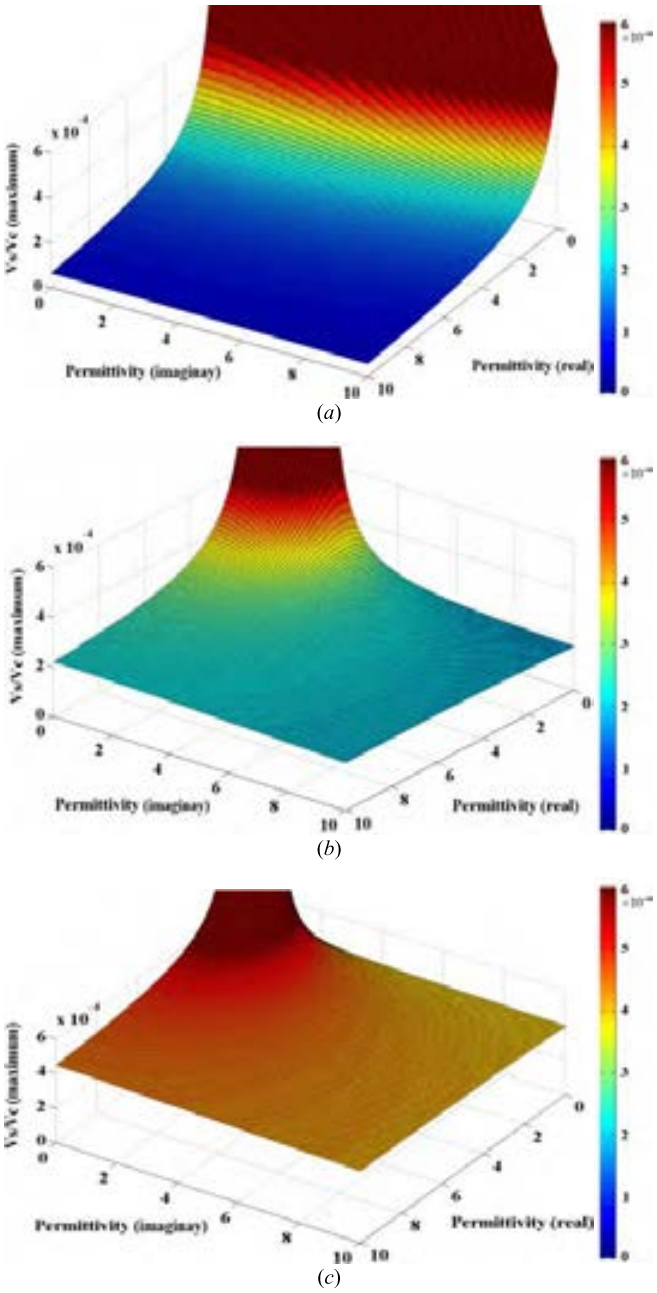

Fig. 5. Maximum sample volume $(V_s/V_c)_{\max}$. (a) Dielectric rod/bar. (b) Dielectric sphere/cube. (c) Dielectric strip/disk.

has already been calculated by demagnetizing cavity modes in [17]

$$\frac{f_0 - f_s}{f_0} = \frac{8a^2}{4a^2 + \lambda_g^2} \cdot \frac{V_S}{V_C} \cdot \frac{N(\mu_r'^2 + \mu_r''^2) + (1 - 2N)\mu_r'^2 + N - 1}{(N\mu_r' - N + 1)^2 + \mu_r''^2 N^2} \le 10^{-3},$$

$$\frac{V_S}{V_C} = \frac{1}{1000\left[\frac{8a^2}{4a^2 + \lambda_g^2} \cdot \frac{N\left(\mu_r'^2 + \mu_r''^2\right) + (1-2N)\mu_r'^2 + N - 1}{\left(N_m\mu_r' - N_m + 1\right)^2 + \mu_r''^2 N_m^2}\right]}. \quad (35)$$

TABLE I
MAXIMUM SAMPLE VOLUME RATIO TO THE CAVITY $(V_s/V_c)_{\max}$ FOR EVALUATE PERMITTIVITY

Sample Shape	Sample Material					
	Al_2O_3 [18]			SiC [19]		
	Reference [12]	Improved	The rate of increase	Reference [12]	Improved	The rate of increase
Rod / Bar	0.0000633	0.0000719	13.58 %	0.0000195	0.0000227	16.65 %
Strip / Disk	0.000563	0.000563	0 %	0.000509	0.000509	0 %
Sphere / Cube	0.000165	0.000230	39.43 %	0.000165	0.000176	6.98 %

By equating the real part of (30) and assuming the same frequency shift range condition as in [12], it can be written as

$$\frac{f_0 - f_s}{f_0} = (\mu_r' - 1)\frac{8a^2}{4a^2 + \lambda_g^2}\frac{V_S'}{V_C} - \frac{2N_m\left[\left((\mu_r'-1)^2 - \mu_r''^2\right)\left(N_m\mu_r' - N_m + 1\right) + 2(\mu_r'-1)\mu_r''^2 N_m\right]}{\left(N_m\mu_r' - N_m + 1\right)^2 + \mu_r''^2 N_m^2} \times \frac{4a^2}{4a^2 + \lambda_g^2}\frac{V_S'}{V_C} \le 10^{-3}. \tag{36a}$$

Thus, the ratio of maximum sample volume to the cavity $(V_s/V_c)_{\max}$ is given by

Similarly, the proposed formula (36) can be used to compare with the reported result in [17], for the complex permeability of magnetite using the demagnetizing factor. The results of plotting $(V_s/V_c)_{\max}$ as a function of complex permeability are shown in Fig. 6. It is noticed that the maximum value of ratio $(V_s/V_c)_{\max}$ as a function of the complex permeability highly depends on the sample geometry. To verify how much the values of ratio $(V_s/V_c)_{\max}$ increased between (35) and (36) from Fig. 6 accurately, we use the magnetic samples $NiFe_2O_4(\mu_r^* = 15.42 - 0.428i)$ at 2.67 GHz and $LiZnFe_2O_3$ $(\mu_r^* = 24.18 - 0.541i)$ at 2.67 GHz [3]. The results in Table II demonstrate the increase in the value of $(V_s/V_c)_{\max}$ used by the proposed rectangular CPT. It is observed that the volume ratio $(V_s/V_c)_{\max}$ is also increased up to almost 39% in the example geometries except for the strip/disk. In the case of the strip/disk, the magnetic material has N value equal to "1." It means that the magnetic material is sufficiently polarized as the inductor in the magnetic field. Therefore, when the disk-shaped sample is sufficiently polarized, the CPT of the reported [17] is also useful. However, if the sample has other shape, we can measure the complex properties of the sample using the proposed rectangular CPT as improving the accuracy.

In Section V, through practical experiments, we prove the proposed technique to draw a broad conclusion. The measurement of resonant frequency and quality factor by utilizing VNA is presented. Moreover, the proposed advanced rectangular CPT is validated using the measured data.

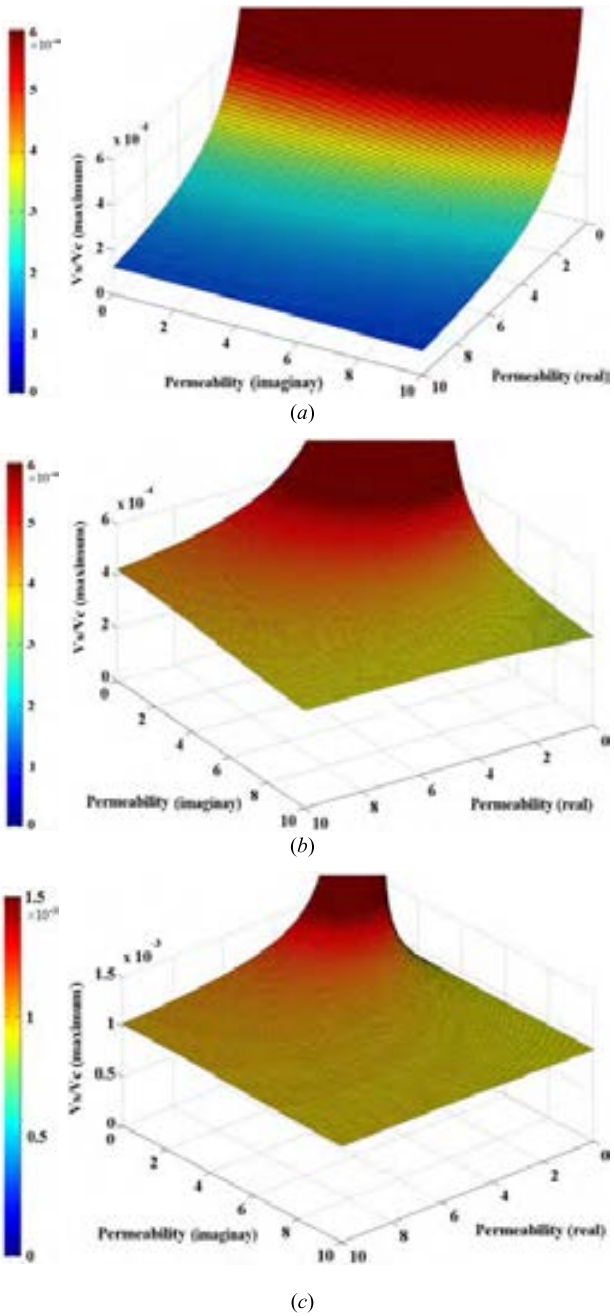

Fig. 6. Maximum sample volume ratio $(V_s/V_c)_{\max}$. (a) Rod/bar of magnetic material. (b) Sphere/cube of magnetic material. (c) Strip/disk of magnetic material. The figures of the maximum sample volume ratio simulated by the ACPT.

V. PRACTICAL EXPERIMENT AND RESULTS ON REAL DATA

A. Data Correction

In the proposed RC perturbation measurement, we use the wooden stickholder to insert or place the sample at the desired position inside the RC for accurate measurement. However, the holder may have susceptibility of complex permittivity and

TABLE II
MAXIMUM SAMPLE VOLUME RATIO TO THE CAVITY $(V_s/V_c)_{\max}$ TO EVALUATE PERMEABILITY

Sample Shape	Sample Material					
	$NiFe_2O_4$			$LiZnFe_2O_3$		
	Reference [3]	The proposed method	The rate of increase	Reference [3]	The proposed method	The rate of increase
Rod / Bar	0.0000961	0.0001193	24.14 %	0.0000598	0.0000830	38.8 %
Strip / Disk	0.0015	0.0015	0 %	0.0014	0.0014	0 %
Sphere / Cube	0.0004734	0.0005773	21.95 %	0.0004665	0.0005215	11.79 %

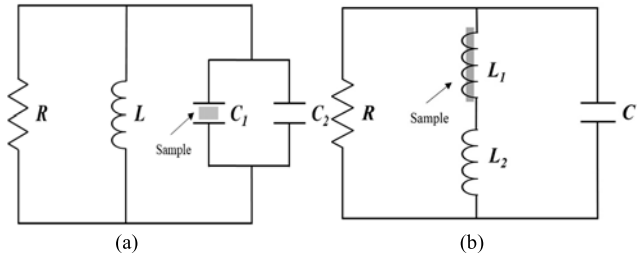

Fig. 7. Lumped-element equivalent circuit of a resonant cavity at resonant mode when a dielectric sample is in (a) maximum electric field [20] and (b) maximum magnetic field.

permeability to change the original sample value. In order to obtain accuracy, we divide the measured data between measuring the sample with holder and without holder. In the data correction procedure, we should satisfy certain conditions. First, the sample is placed at the maximum electric field, which has zero magnetic field for the complex permittivity or at the maximum magnetic field, which has zero electric field for the complex permeability. Second, the width $(w_i, i = 1,2)$ of sample should be much smaller than the guided wavelength to reduce the effect of fringing field [21]. Provided the preconditions, it is reasonable that the inductance and capacitance of the cavity at resonance are unperturbed when the sample is placed in the maximum electric or magnetic fields. We have modeled an equivalent lumped-element circuit at a single resonant frequency, as shown in Fig. 7.

In Fig. 7(a) and (b), the lumped-element equivalent circuits has resonant frequency and quality factor that can be written as [10], [20]

$$f_a = \frac{1}{2\pi\sqrt{L(C_1+C_2)}}, \quad f_b = \frac{1}{2\pi\sqrt{C(L_1+L_2)}} \tag{37a}$$

$$Q = \frac{2\omega \cdot W_{e,m}}{P_d} \tag{37b}$$

where f_a and f_b indicate the resonant frequencies in Fig. 7(a) and (b), respectively, $W_{e,m}$ indicates the accumulated energy of electric or magnetic fields, and P_d indicates the power consumption in the sample.

Based on the evaluation of the parallel lumped-element equivalent circuit, we can eliminate the interference of holder to obtain the resonance frequency and quality factor as [21]

$$\begin{aligned} \omega_{cs}^{-2} &= \omega_{\text{chs}}^{-2} - \omega_{\text{ch}}^{-2} + \omega_c^{-2} = L(C_c + C_s) \\ f_{cs}^{-2} &= f_{\text{chs}}^{-2} - f_{\text{ch}}^{-2} + f_c^{-2} \end{aligned} \tag{38}$$

where L indicates the inductance of the cavity and C indicates the capacitance of the cavity. The subscripts c, ch, and chs indicate the measured parameters from the cavity, the cavity with the holder, and the cavity with the sample on the holder, respectively. In this experiment, we measure the natural resonant frequency of the cavity (ω_c), with the holder (ω_{ch}), and with the sample on the holder (ω_{chs}) and then organize the measured data to derive an expression. The expressions in (38) show the resonant frequency shift between the empty cavity (f_c) and the cavity with only sample (f_{cs}). Likewise, we can also evaluate the quality factor change between the empty cavity and the cavity with only sample. As the power loss and quality factor are in inverse proportion to each other, the quality factor can be verified from the sum of power loss at each situation. We measure the natural quality factor (Q_c^{-1}), the quality factor with holder (Q_{ch}^{-1}), and the quality factor with sample on holder (Q_{chs}^{-1}) to verify the quality factor with only sample as

$$Q_{cs}^{-1} = Q_{\text{chs}}^{-1} - Q_{\text{ch}}^{-1} + Q_c^{-1}. \tag{39}$$

The above-mentioned formulas are approximated because the port coupling might be dependent on the sample insertion. Hence, by using (38) and (39), we can obtain the corrected resonant frequency and quality factor with the sample in the cavity.

B. Measuring Complex Permittivity and Permeability

In this section, we demonstrate the advantage of the proposed rectangular CPT in various sample shapes and volumes

$$\frac{V_S'}{V_C} = \frac{1}{1000\left[\left(\mu_r'-1\right)\frac{8a^2}{4a^2+\lambda_g^2} - \frac{2N_m\left[\left(\left(\mu_r'-1\right)^2-\mu_r''^2\right)\left(N_m\mu_r'-N_m+1\right)+2\left(\mu_r'-1\right)\mu_r''^2N_m\right]}{\left(N_m\mu_r'-N_m+1\right)^2+\mu_r''^2N_m^2}\frac{4a^2}{4a^2+\lambda_g^2}\right]}. \tag{36b}$$

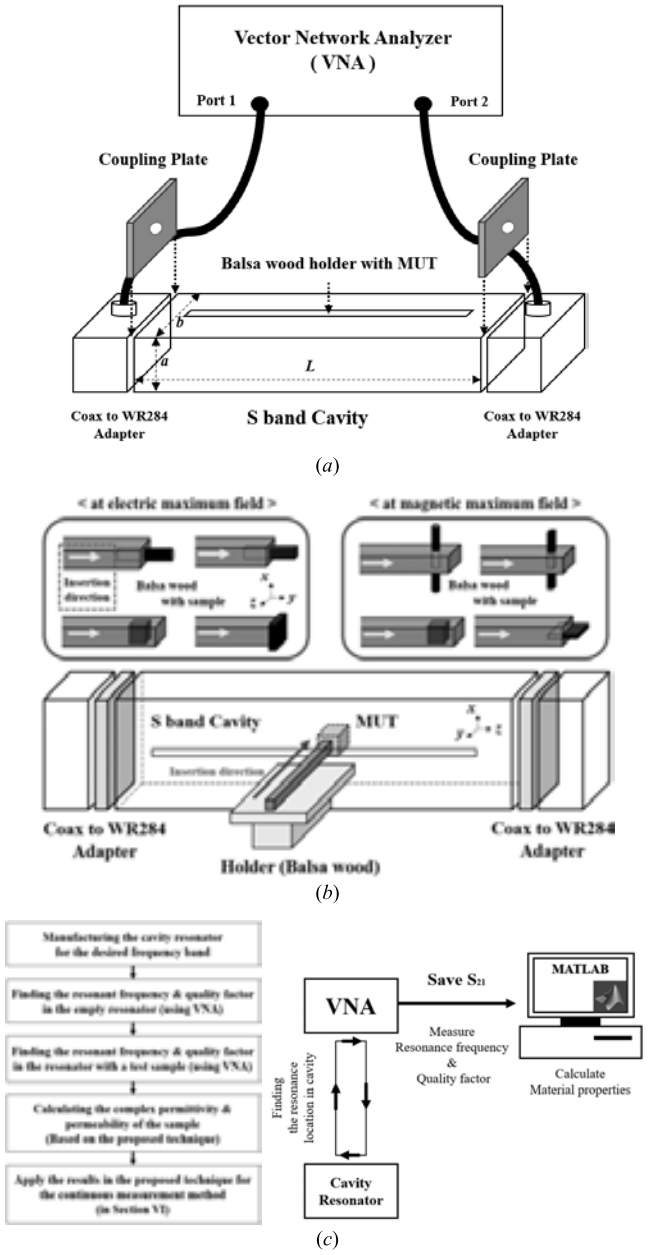

Fig. 8. (a) Detailed system sketch. (b) Measurement setup sketch. (c) Flowchart for the proposed measurement process.

compared with the reference techniques. In Fig. 8(a), the *S*-band WR284 waveguide ($a = 72.18$ mm, $b = 34.16$ mm, and $L = 483$ mm) is fabricated along with aluminum plates placed at both the ends, and the sample insertion slit is made at the centerline of the waveguide. The TE resonant modes in the waveguide can be calculated as [24]

$$f_{mnl} = \frac{ck_{mnl}}{2\pi\sqrt{\mu_r\varepsilon_r}} = \frac{c}{2\pi\sqrt{\mu_r\varepsilon_r}}\sqrt{\left(\frac{m\pi}{a}\right)^2+\left(\frac{n\pi}{b}\right)^2+\left(\frac{l\pi}{L}\right)^2}. \tag{40}$$

Table III illustrates the calculated and measured resonant frequency and measured quality factor at the TE_{10l} mode in the waveguide. It can be noticed from the calculated and measured results that both are reasonably matched for WR-284 waveguide. To calculate accurate complex permittivity and

TABLE III
RESONANT FREQUENCY AND QUALITY FACTOR OF THE WR284 WAVEGUIDE

$TE_{m,n,l}$	f_o [GHz] (Calculated)	f_o [GHz] (Measured)	Q_o (Measured)
$TE_{1,0,5}$	2.602	2.5894	7525
$TE_{1,0,6}$	2.802	2.7849	6995
$TE_{1,0,7}$	3.021	3.0079	6438
$TE_{1,0,8}$	3.255	3.2314	6161
$TE_{1,0,9}$	3.502	3.4745	5204
$TE_{1,0,10}$	3.758	3.7272	3092
$TE_{1,0,11}$	4.023	3.9882	3663

permeability, we utilized the TE_{105} and TE_{106} modes, as they have the highest value of quality factor in the resonant modes. The resonant frequency and the quality factor are obtained from the peak point of the S_{21} parameter. The resonant bandwidth can be measured by VNA (Agilent E8357A), which provides the 3-dB method to obtain the *Q*-factor. Before carrying out the measurement in the fabricated WR-284 cavity under both the loaded and unloaded conditions, the VNA was calibrated by the *S*-band waveguide calibration kit (Agilent 8722ES and 85033D). At each resonant TE mode, we use the maximum sampling points (16 001) of frequency available on the VNA to measure the accurate quality factor and resonant frequency without any curve-fitting technique. In addition, the overall process is illustrated as a flowchart in Fig 8(c). As shown in Fig. 9, we show the electric and magnetic field patterns of the TE_{105} and TE_{106} modes in the *S*-band cavity resonator, respectively. Therefore, the sample, with the help of the balsa holder or glass holder, is placed at the center of the cavity to measure the complex permittivity and permeability.

For verifying the accuracy of the proposed rectangular CPT, we fabricate two rod-/bar-shaped samples having different volumes, disk-shaped samples, and cube-shaped samples, as shown in Fig. 8(b). The four standard-shaped Al_2O_3 [18] are used to measure the complex permittivity in TE_{105}. Also, four standard-shaped YIG [25] are used to measure the complex permeability in TE_{106}. These two materials are also satisfied with a homogenous and isotropic structure. The measured S_{21} curve of the empty cavity and the S_{21} curves for the four type samples are shown in Fig. 10. The resonant frequency is obtained by measuring the peak point of the S_{21} curve, whereas the quality factor is calculated by the 3-dB method for each mode. The calculated results using the measured data are listed in Table IV (located in page 13), where the subscript *ro* indicates the value from the classical CPT and the subscript *ri* and *ra* indicate the values from the previous CPT literature and from the proposed rectangular CPT, respectively. Furthermore, f_s and Q_s are the resonant frequency and the quality factor measured in this experiment, respectively. Our proposed CPT is compared with the previous cavity perturbation calculation techniques [11], [12]. It is found in Table IV that for the full-length rod-/bar-shaped Al_2O_3, the results obtained from

TABLE IV

COMPARISON BETWEEN THE RESULTS FROM THE EXPERIMENT USING THE CPT IN REFERENCE AND THE ADVANCED RECTANGULAR CPT

Sample Shape Al_2O_3 [18]		Sample dimension (mm)	Sample material [18]	f_0 (GHz)	f_S (GHz)	Q_0	Q_S	Classical CPT $\varepsilon'_{ro} - j\varepsilon''_{ro}$	Reported CPT [12] $\varepsilon'_{ri} - j\varepsilon''_{ri}$	The Proposed method $\varepsilon'_{ra} - j\varepsilon''_{ra}$
Rod / Bar	Big	1×1×33.88	Al_2O_3	2.5889599	2.5874779	6655	6200	8.85-j0.005	8.85-j0.005	8.85-j0.005
			$[tan\,\delta_\varepsilon]$		-		-	0.0005	0.0005	0.0005
	Small	1×1×3	Al_2O_3	2.5889599	2.5881786	6655	6372	6.88-j0.100	8.86-j0.179	8.88-j0.006
			$[tan\,\delta_\varepsilon]$	-	-		-	0.0145	0.0202	0.0006
			Error $(\Delta\varepsilon_r^*/\varepsilon_r^*)$ %	-	-		-	22% -j 95%	0.1% -j 97%	0.3% -j 16%
Disk	Big	2.5 (Radius) × 0.5 (Thickness)	Al_2O_3	2.5893542	2.5888782	7665	6452	4.3-j0.009	-0.79-j0.002	8.85-j0.006
			$[tan\,\delta_\varepsilon]$	-	-		-	0.0021	-0.00253	0.0006
			Error $(\Delta\varepsilon_r^*/\varepsilon_r^*)$ %	-	-		-	51% -j 44%	109% -j 16%	0% -j 16%
	Small	2 (Radius) × 0.5 (Thickness)	Al_2O_3	2.5893129	2.5890821	7665	6870	4.16-j0.011	-0.95-j0.004	8.39-j0.006
			$[tan\,\delta_\varepsilon]$	-	-		-	0.0026	-0.0042	0.0007
			Error $(\Delta\varepsilon_r^*/\varepsilon_r^*)$ %	-	-		-	53% -j 55%	111% -j 16%	5% -j 16%
Sphere (N=1/3) /Cube (N=0.26)	Big	4×4×4	Al_2O_3	2.5893129	2.5884376	7650	6828	3.62-j 0.0108	20.48-j0.597	8.80-j0.005
			$[tan\,\delta_\varepsilon]$	-	-		-	0.0034	0.02915	0.00065
			Error $(\Delta\varepsilon_r^*/\varepsilon_r^*)$ %	-	-		-	59% -j 46%	56% -j 99%	0.5% -j 0%
	Small	3×3×3	Al_2O_3	2.589043	2.5886892	6825	6305	3.18- j 0.0105	8.84-j0.136	8.84-j0.005
			$[tan\,\delta_\varepsilon]$	-	-		-	0.0033	0.0154	0.0005
			Error $(\Delta\varepsilon_r^*/\varepsilon_r^*)$ %	-	-		-	64% -j 52%	0.1% -j 96%	0.1% -j 0%

Sample Shape		Sample dimension (mm)	Sample material [25]	f_0 (GHz)	f_S (GHz)	Q_0	Q_S	Classical CPT $\mu'_{ro} - j\mu''_{ro}$	Reported CPT [11] $\mu'_{ri} - j\mu''_{ri}$	The Proposed method $\mu'_{ra} - j\mu''_{ra}$
Rod / Bar	Big	1×1×39.99	YIG	2.7847897	2.7848530	7488	5706	0.024-j0.90	0.027-j0.90	0.027-j0.90
			$[tan\,\delta_\mu]$	-	-	-	-	29.17	33.33	33.33
	Small	1×1×20.01	YIG	2.7847897	2.7848269	7488	6287	0.11-j0.851	0.022-j0.91	0.022-j0.92
			$[tan\,\delta_\mu]$	-	-	-	-	7.74	41.3636	41.81
			Error $(\Delta\mu_r^*/\mu_r^*)$ %	-	-	-	-	78% -j 17%	18% -j 1.1%	18% -j 2%
Disk	Big	2 (Radius) × 0.5 (Thickness)	YIG	2.7847897	2.7847902	7474	7075	0.97-j0.627	0.97-j0.628	0.027-j0.92
			$[tan\,\delta_\mu]$	-	-	-	-	0.646	0.647	33.33
			Error $(\Delta\mu_r^*/\mu_r^*)$ %	-	-	-		97% -j 30%	97% -j 30%	0 % -j 3%
	Small	1.5 (Radius) × 0.5 (Thickness)	YIG	2.7847897	2.7847904	7474	7263	0.93-j0.568	0.93-j0.568	0.028-j0.92
			$[tan\,\delta_\mu]$	-	-	-	-	0.611	0.611	32.857
			Error $(\Delta\mu_r^*/\mu_r^*)$ %	-	-	-	-	98% -j 23%	97% -j 36%	3.5% -j 3%
Sphere (N=1/3) /Cube (N=0.26)	Big	3×3×3	YIG	2.7847897	2.7848359	7474	6765	0.18-j0.346	0.18-j0.347	0.028-j0.92
			$[tan\,\delta_\mu]$	-	-		-	1.922	1.928	32.86
			Error $(\Delta\mu_r^*/\mu_r^*)$ %	-	-		-	86% -j 39%	85% -j 58%	3.5% -j 3%
	Small	1×1×1	YIG	2.7851207	2.7851281	6642	6536	-2.76-j1.72	-2.77-j1.72	0.028-j0.9
			$[tan\,\delta_\mu]$	-	-	-	-	-0.623	-0.621	32.143
			Error $(\Delta\mu_r^*/\mu_r^*)$ %	-	-	-	-	101% -j59%	101% -j48%	3.5% -j 0%

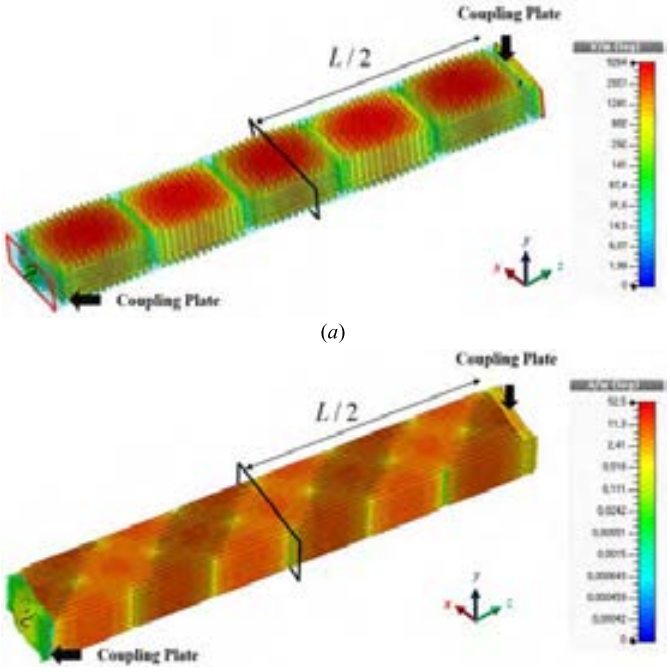

Fig. 9. (a) E-field distribution in TE_{105}. (b) H-field distribution in TE_{106} (units of the electric and magnetic field in log scale).

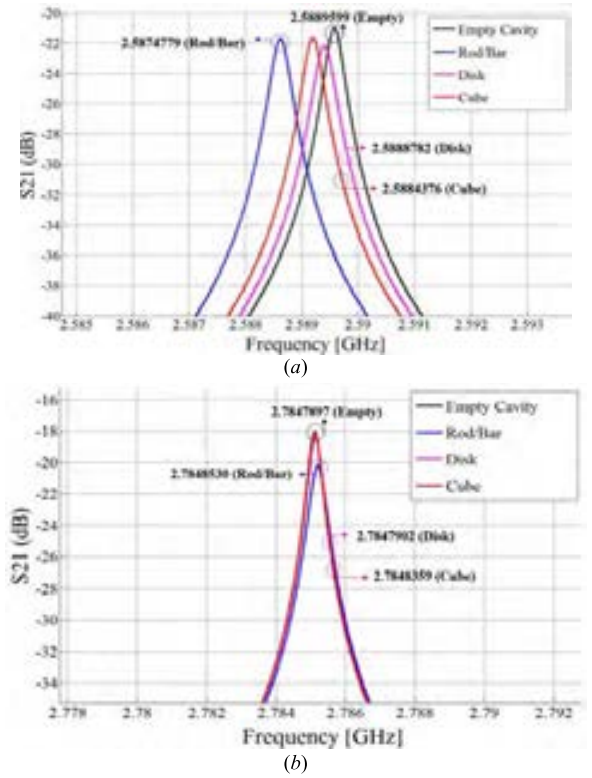

Fig. 10. (a) Measured S-parameter data for various dielectric samples in TE_{105}. (b) Measured S-parameter data for various magnetic samples in TE_{106}. The resonance frequency in Fig. 10 indicates the peak point for each shape.

three methods have the same value as it is the basic sample shape, valid also in the original CPT. However, on the contrary regarding small length rod/bar shape, the imaginary complex permittivity shows noticeable errors, as the sample size gets smaller. It shows that the CPTs, except for the proposed RCPT, are insufficient to evaluate the real and imaginary permittivities because original CPT is not considering the phenomena of the sample at the resonant location inside the resonator. In the reference article [28], they have already shown and analyzed that the complex properties for partial lengths of sample in the cavity were difficult to be measured by conventional CPT. In other shapes (disk and cube), we obtain more accurate complex permittivity values by utilizing the proposed RCPT than other techniques. Compared with previous articles in Table IV, we analyzed in detail the polarization phenomena occurring inside the resonator and calculated the volume of the sample accurately according to the microwave field. Similarly, in case of complex permeability, we also obtain the accurate complex permeability value and report in Table IV, which does not show any change depending on the sample volume and shape, when calculated by the proposed RCPT. For better analyzing the performance, the percentage error rate in the real and imaginary parts of the complex properties is shown in Table IV. The error rates are calculated to compare the value between the original material properties and the proposed material properties of the same shape and size. In previous methods, the error rate is up to 98%, and however, in the proposed method, it has the error rate up to 16%. Although 16% can be seen as an unsatisfied value to a high accuracy. The actual difference between the results is '0.001' which is sufficiently small difference due to the low-loss material. Hence, it can be observed that for the dielectric samples and magnetic samples, the results calculated by the RCPT come out more accurately than the results calculated by the CPT and reported CPT. Using the proposed RCPT, we can get the accurate properties of the sample compared with the previous CPT, in case of all four standard-shaped samples. Throughout the result in Table IV, it is evident that the sample maximum volume can be increased and the sample properties can be measured more accurately with the various shapes of sample using the proposed RCPT. In addition, the CPT, including our proposed method, is mathematically valid not only in the S-band but also in other frequency bands. In other words, based on the proposed method, the complex characteristics of the sample can be measured in various frequency bands. In Section VI, we propose a method to measure the permittivity and permeability of materials at the wide frequency band by the resonators from 2.6 to 13 GHz, which we fabricate for the experiment. Moreover, since the proposed method (29) and (30) derives the permittivity and permeability from the variation of the resonant frequency and the variation of the Q-factor, we can also obtain the accurate calculation results by the resonator at over 13 GHz.

VI. Application Technique for Proposed Method (Continuous Measurement Method)

In the conventional perturbation method, it is required to measure the sample by changing the location and position of material for a specific frequency. However, based on the result of the cube-type sample in the proposed method, we can

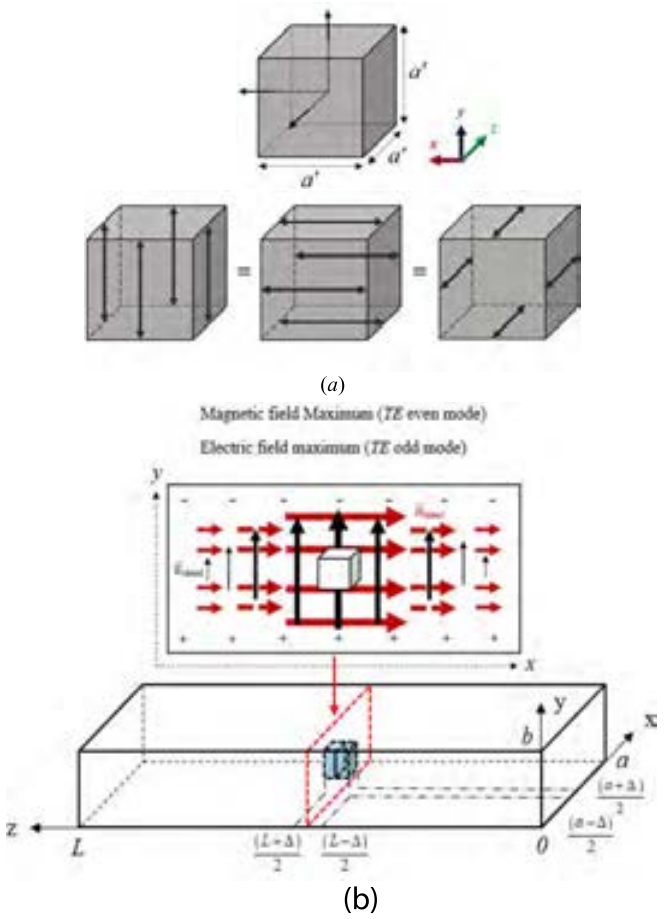

Fig. 11. (a) Cube-shaped sample's geometry effects, when measured in the electromagnetic field of x, y, and z. (b) Example of the cube-type sample placed in the electromagnetic maximum field of the TE_{10p} mode inside the *RC* when measured by the proposed method.

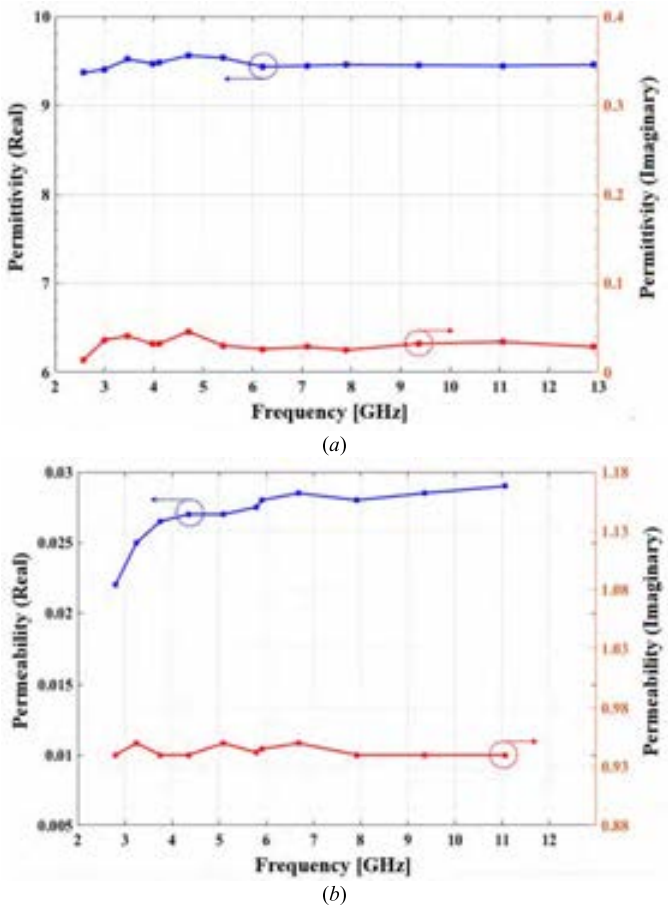

Fig. 12. (a) Measured complex permittivity (Al_2O_3). (b) Complex permeability (YIG) data from 2.5 to 13 GHz.

Fig. 13. Picture of (a) cube-shaped Al_2O_3 and (b) cube-shaped SiC, used in the proposed measurement method.

continuously measure the material's complex properties in a desired frequency range without changing the location and position. Among the analyzed sample's shapes, the cube-shaped sample receives the same size field in all directions, as shown in Fig. 11(a). Also, at the center of the RC, the resonance points of both the odd and even modes of TE are present at the same time, as shown in Fig. 11(b). It means that we can measure the complex permittivity and permeability of the sample without any physical relocation not only at specific frequency but also in a desired frequency bandwidth. Therefore, to verify the continuous measurement, we need to calculate the volume and depolarization factor "N" of cube-type sample and assign it to (29) and (30) with the RC structures corresponding to the desired frequency band. From (10) and (11) in condition of the cube shape at the maximum E- and H-fields, respectively, the valid volumes of the cube-shaped sample can be written as

$$V_S' = a'\left(\frac{a'}{2} + \frac{a}{2\pi}\sin\left(\frac{\pi a'}{a}\right)\right)\left(\frac{a'}{2} + \frac{L}{2\pi n}\sin\left(\frac{n\pi a'}{L}\right)\right) \tag{41}$$

$$V_S' = \frac{a'^3}{4}\left(1 + \frac{\sin(k_x a')}{k_x a'}\right)\left(1 + \frac{\sin(k_z a')}{k_z a'}\right). \tag{42}$$

From (26), the effective depolarizing factor "N" can be introduced according to the specification of the cube-shaped sample and RC in Table IV. For measuring the continuous complex permittivity and permeability in the proposed rectangular CPT, we use cube-shaped Al_2O_3 [18] and YIG [25], which have been verified in Section V. Also, we fabricate WR-284 (2.6–3.95 GHz), WR-187 (3.95–5.85 GHz), WR-159 (4.64–7.2 GHz), and WR-90 (8.2–12.4 GHz) for wideband frequency range from 2.5 to 13 GHz, as shown in Fig. 14. Based on the proposed CPT in Section III, the complex permittivity and permeability can be measured in the odd and even modes of TE, respectively. Table V summarizes the resonance frequency and the quality factor in each mode

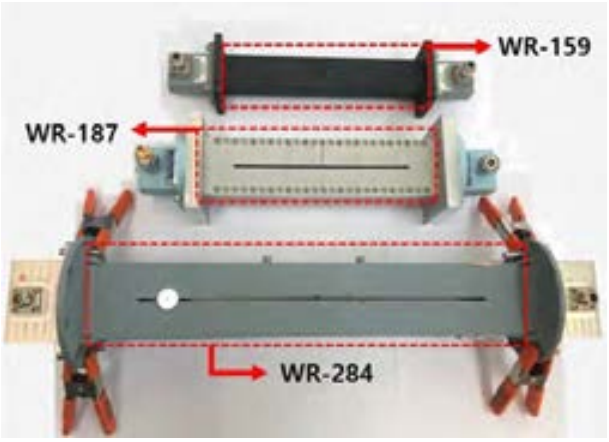

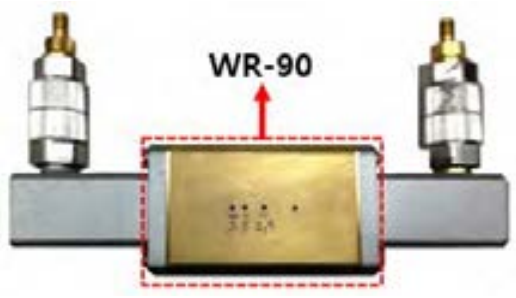

(*a*)

(*b*)

Fig. 14. (a) Picture of WR-90, WR-158, WR-187, and WR-284, used in measurement. (b) Picture of measurement setup in the experiment.

with the RCs. As a result of substituting the resonance frequency and quality factor of Al_2O_3 and YIG into (29) and (30), respectively, the complex permittivity of Al_2O_3 and the complex permeability of YIG can be obtained efficiently from 2 to 12 GHz. Through the result in Fig. 12, it is evident that the complex properties of the sample can be measured consistently with the cube shape.

VII. Conclusion

In this article, we have demonstrated that the proposed method has the advantage compared to the conventional CPT in terms of accuracy, sample size limitation, and physical relocation. Moreover, it leads to reduce the uncertainty of the conventional method. Material samples that could not satisfy the shape and length condition at the desired frequency due to the difficulty in material processing could not be measured with conventional CPT accurately. We can measure such material properties using the proposed method more accurately. To overcome the previous research, we analyzed two aspects of the electromagnetic field in a sample under measurement. First, we calculated the valid sample volume in the maximum electric and magnetic fields. Second, we individually analyzed the uniform field of RC and the depolarized field that occurred when the sample is inserted in the cavity. From these analyses, we applied them to the perturbation theory and proposed a more precise method for measuring the material's complex properties.

By utilizing the proposed technique, a test sample size is not required to match the waveguide size and to be of a particular shape. The three-shaped and different size samples were measured to verify the proposed technique. Based on the resonance frequency and quality factor of the measurement, it was confirmed that the properties calculated by the proposed technique were remarkably close to the reference properties. In addition, it has been observed from the simulation results that with different sample shapes, there is an expansion of the maximum sample volume up to 40% with the proposed method. This proposed technique allows us to become more variable from the constraints of the shape and size of the measurement sample.

Moreover, applying the proposed technique to the cube-shaped sample, we were able to measure the complex properties in the wide frequency band, continuously, without any

TABLE V
Resonant Frequency and Quality Factor

$TE_{m,n,l}$	f_o [GHz]	Q_o	Waveguide Type ($x \times y \times z$ [mm])
$TE_{1,0,5}$	2.602	7525	WR-284 (34.16×72.18×483)
$TE_{1,0,6}$	2.802	6995	
$TE_{1,0,7}$	3.021	6438	
$TE_{1,0,8}$	3.255	6161	
$TE_{1,0,9}$	3.502	5204	
$TE_{1,0,10}$	3.758	3092	
$TE_{1,0,11}$	4.023	3663	
$TE_{1,0,5}$	4.109	3251	WR-187 (22.15×47.55×300)
$TE_{1,0,6}$	4.3503	3221	
$TE_{1,0,7}$	4.704	3056	
$TE_{1,0,8}$	5.0907	2997	
$TE_{1,0,9}$	5.484	4132	
$TE_{1,0,10}$	5.9079	3746	
$TE_{1,0,8}$	5.7931	4021	WR-159 (20.1×40.3×270)
$TE_{1,0,9}$	6.211	3867	
$TE_{1,0,10}$	6.6825	3450	
$TE_{1,0,11}$	7.130	3000	
$TE_{1,0,2}$	7.916	3272	WR-90 (10.16×22.86×66.74)
$TE_{1,0,3}$	9.362	3264	
$TE_{1,0,4}$	11.072	3283	
$TE_{1,0,5}$	12.946	3278	

For Complex Permittivity:

$$\frac{f_0 - f_s}{f_0} = \left[(\varepsilon_r' - 1) - \frac{2N_e \left[\left((\varepsilon_r' - 1)^2 - \varepsilon_r''^2 \right) (N_e \varepsilon_r' - N_e + 1) + 2(\varepsilon_r' - 1)\varepsilon_r''^2 N_e \right]}{(N_e \varepsilon_r' - N_e + 1)^2 + \varepsilon_r''^2 N_e^2} \right] 2\frac{V_S'}{V_C}$$

$$\frac{1}{Q_s} - \frac{1}{Q_0} = \left[\varepsilon_r'' - \frac{N_e \left[\left((\varepsilon_r' - 1)^2 - \varepsilon_r''^2 \right) N_e \varepsilon_r'' - 2(\varepsilon_r' - 1)\varepsilon_r'' (N_e \varepsilon_r' - N_e + 1) \right]}{(N_e \varepsilon_r' - N_e + 1)^2 + \varepsilon_r''^2 N_e^2} \right] 4\frac{V_S'}{V_C}.$$

For Complex Permeability:

$$\frac{f_0 - f_s}{f_0} = \left[(\mu_r' - 1) - \frac{N_m \left[\left((\mu_r' - 1)^2 - \mu_r''^2 \right) (N_m \mu_r' - N_m + 1) + 2(\mu_r' - 1)\mu_r''^2 N_m \right]}{(N_m \mu_r' - N_m + 1)^2 + \mu_r''^2 N_m^2} \right] \frac{8a^2}{4a^2 + \lambda_g^2} \frac{V_S'}{V_C}$$

$$\frac{1}{Q_S} - \frac{1}{Q_0} = \left[\mu_r'' - \frac{N_m \left[\left((\mu_r' - 1)^2 - \mu_r''^2 \right) N_m \mu_r'' - 2(\mu_r' - 1)\mu_r'' (N_m \mu_r' - N_m + 1) \right]}{(N_m \mu_r' - N_m + 1)^2 + \mu_r''^2 N_m^2} \right] \frac{16a^2}{4a^2 + \lambda_g^2} \frac{V_S'}{V_C}.$$

TABLE VI
RESONANT FREQUENCY AND QUALITY FACTOR WITH HOLDER

- BIG SIZE AL_2O_3 ROD / BAR-

TE_{mnl}	f_h [GHz]	Q_h [GHz]
TE_{105}	2.5882319	6381

- SMALL SIZE AL_2O_3 ROD / BAR-

TE_{mnl}	f_h [GHz]	Q_h [GHz]
TE_{105}	2.5882319	6381

- BIG SIZE AL_2O_3 DISK-

TE_{mnl}	f_h [GHz]	Q_h [GHz]
TE_{105}	2.5890195	6465

- SMALL SIZE AL_2O_3 DISK-

TE_{mnl}	f_h [GHz]	Q_h [GHz]
TE_{105}	2.589168634	6881

- BIG SIZE AL_2O_3 CUBE-

TE_{mnl}	f_h [GHz]	Q_h [GHz]
TE_{105}	2.5891686	6828

- SMALL SIZE AL_2O_3 CUBE-

TE_{mnl}	f_h [GHz]	Q_h [GHz]
TE_{105}	2.5889452	6343

- BIG SIZE YIG ROD / BAR-

TE_{mnl}	f_h [GHz]	Q_h [GHz]
TE_{105}	2.7847897	7488

- SMALL SIZE YIG ROD / BAR-

TE_{mnl}	f_h [GHz]	Q_h [GHz]
TE_{105}	2.78847897	7484

- BIG SIZE YIG DISK-

TE_{mnl}	f_h [GHz]	Q_h [GHz]
TE_{105}	2.7847894	7471

- SMALL SIZE YIG DISK-

TE_{mnl}	f_h [GHz]	Q_h [GHz]
TE_{105}	2.7847897	7471

- BIG SIZE YIG CUBE-

TE_{mnl}	f_h [GHz]	Q_h [GHz]
TE_{105}	2.7847897	7471

- SMALL SIZE YIG CUBE-

TE_{mnl}	f_h [GHz]	Q_h [GHz]
TE_{105}	2.7851207	6642

physical relocation. We showed that the results calculated by the proposed technique were remarkably close to the accepted reference value through wideband, as can be found in the literature.

This continuous measurement method proposed in this article is a breakthrough technique that goes beyond the disadvantages of the conventional cavity perturbation method due to obtaining results at specific frequency with physical relocation of samples in different points of RC.

The proposed technique is more accurate and quite reasonable compared with the previous cavity perturbation method for the microwave characterization of dielectric and magnetic samples at wide frequency band more easily and comfortably.

APPENDIX A

To evaluate the resonant frequency and quality factor for the properties of the sample under test, we show the cavity values with holder in Table VI.

APPENDIX B

Complex permittivity and complex permeability are shown at the top of this page.

REFERENCES

[1] D. M. Pozar, *Microwave Engineering*, 3rd ed. New York, NY, USA: Wiley, 1989.

[2] R. A. Waldron, "Perturbation theory of resonant cavities," *Proc. IEE C Monogr.*, vol. 107, no. 12, pp. 272–274, Sep. 1960.

[3] U. Raveendranath and K. T. Mathew, "New cavity perturbation technique for measuring complex permeability of ferrite materials," *Microw. Opt. Technol. Lett.*, vol. 18, no. 4, pp. 241–243, Jul. 1998.

[4] R. B. Yang, C. Y. Tsay, D. S. Hung, W. F. Liang, Y. D. Yao, and C. K. Lin, "Complex permittivity and permeability of iron-based composite absorbers measured by cavity perturbation method in X-band frequency range," *J. Appl. Phys.*, vol. 105, no. 7, Apr. 2009, Art. no. 07A528.

[5] M. Lin, Y. Wang, and M. N. Afsar, "Precision measurement of complex permittivity and permeability by microwave cavity perturbation technique," in *Proc. Joint 30th Int. Conf. Infr. Millim. Waves*, Williamsburg, VA, USA, Sep. 2006, pp. 62–63.

[6] H. B. G. Casimir, "On the theory of electromagnetic waves in resonant cavities," Cornell Univ., Ithaca, NY, USA, Tech. Rep. 6, 1951.

[7] H. Kurss and W. Kahn, "A note on reflector arrays," *IEEE Trans. Antennas Propag.*, vol. 15, no. 5, pp. 692–693, Sep. 1967.

[8] D. Higginbottom, M. Howes, and J. Richardson, "An experimental technique to evaluate the complex permittivity of small samples of microwave substrates," in *Proc. 16th Eur. Microw. Conf.*, Oct. 1986, pp. 790–795.

[9] R. Thomas and D. Dube, "Extended technique for complex permittivity measurement of dielectric films in the microwave region," *Electron. Lett.*, vol. 33, no. 3, p. 218, Jan. 1997.

[10] K. Sudheendran, D. Pamu, M. Ghanashyam Krishna, and K. James Raju, "Determination of dielectric constant and loss of high-K thin films in the microwave frequencies," *Measurement*, vol. 43, no. 4, pp. 556–562, May 2010.

[11] A. K. Jha and M. J. Akhtar, "An improved rectangular cavity approach for measurement of complex permeability of materials," *IEEE Trans. Instrum. Meas.*, vol. 64, no. 4, pp. 995–1003, Apr. 2015.
[12] Z. Peng, J.-Y. Hwang, and M. Andriese, "Maximum sample volume for permittivity measurements by cavity perturbation technique," *IEEE Trans. Instrum. Meas.*, vol. 63, no. 2, pp. 450–455, Feb. 2014.
[13] M. Lin and M. Afsar, "A new cavity perturbation technique for accurate measurement of dielectric parameters," in *IEEE MTT-S Int. Microw. Symp. Dig.*, Jun. 2006, pp. 1630–1633.
[14] S. B. Jones and S. P. Friedman, "Particle shape effects on the effective permittivity of anisotropic or isotropic media consisting of aligned or randomly oriented ellipsoidal particles," *Water Resour. Res.*, vol. 36, no. 10, pp. 2821–2833, Oct. 2000.
[15] R. M. Bozorth and D. M. Chapin, "Demagnetizing factors of rods," *J. Appl. Phys.*, vol. 13, no. 5, pp. 320–326, May 1942.
[16] A. Parkash, J. Vaid, and A. Mansingh, "Measurement of dielectric parameters at microwave frequencies by cavity-perturbation technique," *IEEE Trans. Microw. Theory Techn.*, vol. 27, no. 9, pp. 791–795, Sep. 1979.
[17] J. A. Cuenca, S. Klein, R. Ruger, and A. Porch, "Microwave complex permeability of magnetite using non-demagnetising and demagnetising cavity modes," in *Proc. 44th Eur. Microw. Conf.*, Oct. 2014, pp. 128–131.
[18] R. M. Hutcheon, M. S. de Jong, F. P. Adams, P. G. Lucuta, J. E. McGregor, and L. Bahen, "RF and microwave dielectric measurements to 1400°C and dielectric loss mechanisms," in *Proc. Mater. Res. Soc. Symp.*, vol. 269, 1992, pp. 541–551.
[19] A. Chatterjee, T. Basak, and K. G. Ayappa, "Analysis of microwave sintering of ceramics," *AIChE J.*, vol. 44, no. 10, pp. 2302–2311, Oct. 1998.
[20] L. Chen, C. Ong, and B. Tan, "Amendment of cavity perturbation method for permittivity measurement of extremely low-loss dielectrics," *IEEE Trans. Instrum. Meas.*, vol. 48, no. 6, pp. 1031–1037, Dec. 1999.
[21] N. D. Orloff, J. Obrzut, and C. J. Long, "Dielectric characterization by microwave cavity perturbation corrected for nonuniform fields," *IEEE Trans. Microw. Theory Tech.*, vol. 62, no. 9, pp. 2149–2159, Sep. 2014.
[22] A. Kumar and G. Singh, "Measurement of dielectric constant and loss factor of the dielectric material at microwave frequencies," *Pier*, vol. 69, pp. 47–54, 2007.
[23] V. Murthy and R. Raman, "A method for the evaluation of microwave dielectric and magnetic parameters using rectangular cavity perturbation technique," *Solid State Commun.*, vol. 70, no. 8, pp. 847–850, May 1989.
[24] R. F. Harrington, *Time-Harmonic Electromagnetic Fields*. New York, NY, USA: McGraw-Hill, 1961.
[25] D. Ionescu and M. Kovaci, "Performances of the planar ferrite phase shifters based on microwave garnets," in *Proc. 11th Int. Symp. Electron. Telecommun. (ISETC)*, Nov. 2014, pp. 1–4.
[26] M. Santra and K. Limaye, "Estimation of complex permittivity of arbitrary shape and size dielectric samples using cavity measurement technique at microwave frequencies," *IEEE Trans. Microw. Theory Techn.*, vol. 53, no. 2, pp. 718–722, Feb. 2005.
[27] V. Mangulis, *Handbook of Series for Scientists and Engineers*. New York, NY, USA: Academic, 1965.
[28] A. Verma and D. Dube, "Measurement of dielectric parameters of small samples at X-band frequencies by cavity perturbation technique," *IEEE Trans. Instrum. Meas.*, vol. 54, no. 5, pp. 2120–2123, Oct. 2005.
[29] A. K. Jha and M. J. Akhtar, "A generalized rectangular cavity approach for determination of complex permittivity of materials," *IEEE Trans. Instrum. Meas.*, vol. 63, no. 11, pp. 2632–2641, Nov. 2014.

Chul-Ki Kim was born in Gangneung, South Korea, in July 1989. He received the B.S. degree in electronic engineering from Soongsil University, Seoul, South Korea, in 2014, and the M.S. degree in electrical engineering from the Korea Advanced Institute of Science and Technology, Daejeon, South Korea, in 2016, where he is currently pursuing the Ph.D. degree in electrical engineering.

His current research interests include microwave perturbation and synthetic aperture radar.

Laxmikant Minz was born in Katihar, India, in 1986. He received the B.Tech. degree in electronic and communication engineering from NIT Nagpur, Nagpur, India, in 2007, and the M.Tech. degree in RF and microwave engineering from IIT Kharagpur, Kharagpur, India, in 2009. He is currently pursuing the Ph.D. degree with the School of Electrical Engineering, Korea Advanced Institute of Science and Technology, Daejeon, South Korea.

His current research interests include metamaterials, antenna design, and microwave circuit design.

Seong-Ook Park (Senior Member, IEEE) was born in Kyungpook, South Korea, in December 1964. He received the B.S. degree from Kyungpook National University, Daegu, South Korea, in 1987, the M.S. degree from the Korea Advanced Institute of Science and Technology, Daejeon, South Korea, in 1989, and the Ph.D. degree from Arizona State University, Tempe, AZ, USA, in 1997, all in electrical engineering.

From March 1989 to August 1993, he was a Research Engineer with Korea Telecom, Daejeon, working on microwave systems and networks. He later joined the Telecommunication Research Center, Arizona State University, until September 1997. Since October 1997, he has been with the Information and Communications University, Daejeon. He is currently a Professor with the Korea Advanced Institute of Science and Technology. His research interests include mobile handset antenna and analytical and numerical techniques in the area of electromagnetics.

Dr. Park is a member of Phi Kappa Phi.